

# INFRARED ECHOES REVEAL THE SHOCK BREAKOUT OF THE CAS A SUPERNOVA

Eli Dwek<sup>1</sup> and Richard G. Arendt<sup>2</sup>

## ABSTRACT

The serendipitous discovery of infrared echoes around the supernova remnant of Cas A by the *Spitzer* satellite has provided astronomers with a unique opportunity to study the properties of the echoing material and the history and nature of the outburst that generated these echoes. In retrospect, the echoes are also clearly visible as infrared “hot spots” in *IRAS* images of the region. In this paper we present a detailed analysis of the geometry and spectra of the echoes, and the nature of the radiation source that created them. We rule out a suggestion, based on early and spatially-limited data, that the echoes were generated by a recent pulse of radiation that occurred around 1950. All the echoes located within a distance of  $\sim 15'$  from the SN are caused by the delayed arrival of thermal emission from dust located at a distance of 160 lyr (corresponding to half the adopted age of the remnant) directly behind the origin of the explosion. The spectra of the echoes are distinct from that of the general diffuse interstellar medium (ISM) revealing hot silicate grains that are either stochastically heated to temperatures in excess of  $\sim 150$  K, or radiating at an equilibrium temperature of this value. We show that the optical light curve from the supernova, is not capable of producing such spectra, and could therefore not have given rise to the echoes. Instead, we find that the echoes were generated by an intense and short burst of EUV-UV radiation associated with the breakout of the shock through the surface of the exploding star. The inferred luminosity of the burst depends on the amount of attenuation in the intervening medium to the clouds, and we derive a burst luminosity of  $\sim 1.5 \times 10^{11} L_{\odot}$  for an assumed H-column density of  $1.5 \times 10^{18} \text{ cm}^{-2}$ . The average H-column density of the IR emitting region in the echoing clouds is about  $5 \times 10^{17} \text{ cm}^{-2}$ . Derivation of their density requires knowledge of the width of the echo that is sweeping through the ISM, which in

---

<sup>1</sup>Observational Cosmology Lab., Code 665; NASA Goddard Space Flight Center, Greenbelt, MD 20771, U.S.A., e-mail: eli.dwek@nasa.gov

<sup>2</sup>University of Maryland Baltimore County (UMBC), Code 665, NASA Goddard Space Flight Center, Greenbelt MD, 20771, U.S.A., e-mail: richard.g.arendt@nasa.gov

turn is determined by the duration of the burst. Taking a burst time of  $\sim 1$  d gives a cloud density of  $\sim 400 \text{ cm}^{-3}$ , typical of dense IR cirrus.

*Subject headings:* ISM: supernova remnants – ISM: individual (Cassiopeia A) – ISM: interstellar dust – Infrared: general

## 1. INTRODUCTION

Short-lived luminous sources can produce echoes of their outburst in the ISM. These echoes can be manifested as line emission from the gas, or reflected and thermally-reradiated light from the dust in the ISM. They can be used to probe the morphology of the interstellar medium (ISM) through which they are expanding and to reconstruct the historical record of the temporal behavior of the light source.

Visible light echoes have been detected around Nova Persei 1901 (Kapteyn 1902; Bode et al. 2004), V838 Mon (Bond et al. 2003), and SN 1987A (Crotts 1988). Fluorescent echoes arising from the equatorial ring around SN1987A have been used to probe the early hours of the burst from the SN, the radius of the ring, and the distance to the LMC (Fransson & Lundqvist 1989; Panagia et al. 1991; Dwek & Felten 1992). The SuperMACHO project has discovered three additional sets of light echoes in the LMC which can be traced back to known supernova remnants (SNRs), and were used to derive ages of 610 and 410 yr for two of the SNRs (Rest et al. 2005).

One of the most unexpected discoveries made by *Spitzer* satellite has been the serendipitous detection of infrared (IR) light echoes in the vicinity of the Cas A SNR. Cas A is the remnant of a supernova that exploded  $\sim 320$  yr ago in the Perseus Arm of the Galaxy, 3.5 kpc away. The echoes were first (and best) detected in 24  $\mu\text{m}$  MIPS scans of Cas A (Fig. 1). Subsequent observations revealed that the echoes are also visible in all IRAC channels and ground-based  $K$  band observations. The echoes vary on time scales of  $< 6$  months, and extend at least  $1.5^\circ$  from the SNR (Hines et al. 2004; Krause et al. 2005; Kim et al. 2008).

Working with the limited, earliest data, Krause et al. (2005) proposed that the echoes are the result of a recent flaring of the neutron star left behind by the SN explosion, instead of the result of a radiative outburst associated with the SN explosion. More recently, Kim et al. (2008) have used the 24  $\mu\text{m}$  maps of the echoes over a three year interval to probe the structure of the ISM around Cas A, revealing its complex filamentary structure.

In this paper we combine early spectral observations with more recent data, that have revealed a wider extent of the echoes, to provide a detailed analysis of the epoch and nature

of the radiative burst that gave rise to the echoes, and the density of the interstellar clouds giving rise to the echoes.

We first present a brief description of the discovery of the echoes around Cas A, and derive the IR spectrum of select echoing clouds spanning a wide range of angular distances from the SNR (§2). We also provide a brief mathematical review of the geometry of an echo, and derive the distances of the echoing clouds from the center of the explosion as a function of the epoch at which the burst took place. In §3 we present the model input parameters: the burst delay time and its spectral characteristics, and the interstellar dust model used in the calculations. A stochastic heating model was used to calculate the thermal emission from the dust exposed to the burst of radiation, and in §4 we describe the dependence of the calculated IR fluxes on the burst characteristics. The model fits are then used to derive the properties of the burst and the echoing clouds (§5). The results of our paper are briefly summarized in §6.

## 2. THE INFRARED ECHOES AROUND CAS A

### 2.1. The Discovery of the Echoes

The initial MIPS 24  $\mu\text{m}$  observations (a  $0^\circ.2 \times 0^\circ.3$  scan map) of Cas A serendipitously revealed “chains of IR knots” extending up to  $\sim 12'$  from the center of the SNR (Hines et al 2004). The team followed up with ground-based K band (2.2  $\mu\text{m}$ ) observations which revealed extremely high proper motions of the features. This motivated a second epoch of MIPS 24  $\mu\text{m}$  observation that confirmed that much of the small scale structure outside of the Cas A SNR was changing on time scales of several months (Krause et al. 2005). With these data Krause et al. (2005) proposed that the emission was the echo of a flare of the Cas A neutron star. Assuming that the chains of emission represented a bipolar jet, they deduced that the flare occurred at A.D.  $1952.9 \pm 2.5$ , and it was oriented nearly in the plane of the sky.

Subsequent MIPS 24  $\mu\text{m}$  observations have been repeated at roughly 6 month intervals, and have been expanded to include at first a  $\sim 1$  square degree field around the SNR, and later a  $\sim 9$  square degree field. Examination of these data from the Spitzer archive reveal that echoes are not restricted to the bipolar structure originally detected. They are found at all position angles with respect to the SNR and extend at least  $1^\circ.8$  from the SNR (limited by the size of the map).

Follow-up observations of the echoes also included low and high resolution IRS observations of a bright echo in a filament located  $0^\circ.8$  from the center of the SNR. Additional low

resolution spectra were collected for outlying regions in the vicinity of the SNR. Two of the closest regions to the SNR, located within the NE jet of ejecta and the SW counter jet, have emission lines and the  $22\ \mu\text{m}$  silicate feature that are characteristic of ejecta material. Spectra of other regions exhibited a flat continuum and coincide with highly variable features, and are therefore assumed to be representative echo spectra.<sup>1</sup>

The discovery of the echoes with the *Spitzer* led us to examine if the echoes could also be identified (in hindsight) in the map of the Cas A region that was obtained in 1983 with the *Infrared Astronomical Satellite (IRAS)*. Figure 2 (left panel) shows a false color image at 12, 25, and  $60\ \mu\text{m}$  of the reprocessed *IRAS* map of Cas A and its environment. The emission is dominated by cool interstellar dust grains, peaking at wavelengths of  $\sim 100 - 140\ \mu\text{m}$  (red regions in the image). However, there are several regions with excess  $25\ \mu\text{m}$  emission (including Cas A itself) from hot dust, which thus appear green (Fig. 2, left panel). Comparison to the  $24\ \mu\text{m}$  MIPS data, smoothed to *IRAS* resolution, clearly shows that the  $25\ \mu\text{m}$  excess features are echoes which have moved between 1983 and 2003. The fact that many echoes are in similar locations indicates that many of the clouds producing the echoes are structures that extend for at least 20 lyr along the line of sight. *IRAS* and *Spitzer* have observed different portions of these large-scale structures.

## 2.2. The IR Spectrum of Select Echoes

For the purpose of this work we have concentrated on the analysis of six IR knots that were identified as echoes and have been the target of IRS observations. A seventh  $24\ \mu\text{m}$  echo, without a spectrum, is also included as a representative of the most distant echoing cloud. The selected echoes, listed in Table 1 and as shown in Figure 1, sample a range of angular distances from the nominal center of the explosion. The SL+LL IRS spectra of these echoes were collected from the *Spitzer* archive.<sup>2</sup> Because there are often several sources or extended emission within the slits, we have reprocessed the basic calibrated data (BCD) using the SSC tools *IRS\_CLEANMASK* and *SPICE*. The off-target subslit positions were used to subtract background emission for the corresponding on-target position. In a few cases where the off-target subslit position crossed the SNR, a clean subslit position from an alternate target was used. Both SL and LL data were processed, although in most cases

---

<sup>1</sup>Archival MIPS images were obtained from *Spitzer* programs PID = 718, 30571 – G. Rieke, and PID = 231, 233, 20381 – O. Krause.

<sup>2</sup>Archival IRS spectra were obtained from *Spitzer* programs PID = 3310 – L. Rudnick, and PID = 20381 – O. Krause.

the SL integration times were too short to detect the echoes, which are visible in all IRAC bands. Therefore the analysis presented here relies only on the LL spectra. Figure 3 presents the  $\sim 14 - 40 \mu\text{m}$  spectra of the echoes listed in Table 1.

All echos within a  $1000''$  of Cas A exhibit a steep rise in their spectrum between  $\sim 14 - 20 \mu\text{m}$ , not seen in any IR spectra from the general diffuse ISM. This spectral characteristic provides important clues on the nature of the emitting dust, strongly constraining the viability of different echo models. At longer wavelengths the echoes exhibit subtle differences in the slope of their spectra, suggesting variations in the temperature of the grains in the different echoes. Echo 6 is brighter than the echoes closer to the SNR, and is part of a large extended structure that can be seen in the older IRAS data. This region appears to contain a non-variable emission component which would simply be the same cloud(s) illuminated by the diffuse interstellar radiation field. We have therefore subtracted a scaled ISM spectrum from the Echo 6 spectrum such that its  $20 - 35 \mu\text{m}$  slope is within the range of the slopes of the other echo spectra. This non-variable component accounted for 20 – 50% of the  $20 - 35 \mu\text{m}$  emission.

### 2.3. The Location of the Echoes

We assume that the echoes are the reradiated thermal emission from dust heated by the UV-visual output from the SN, located at point  $S$  (see Figure 4). The emission from dust located at point  $C$  will be detected by an observer at point  $O$  with a delay time  $t$  given by  $ct = r + x - d$ , where  $r$  and  $x$  are, respectively, the distances of  $C$  from the source and the observer, and  $d = \overline{OS}$  is the distance of the observer to the source. The locus of all points with equal delay time is an ellipsoid with the source and the observer at the focal points.

Using the law of cosines:  $r^2 = x^2 + d^2 - 2xd\cos(\alpha)$ , we can express the distance  $r$  in terms of the delay time  $t$  and source distance  $d$  as:

$$r = \frac{d(d + ct)(1 - \cos(\alpha)) + (ct)^2/2}{d(1 - \cos(\alpha)) + ct} \quad (1)$$

where  $\alpha$  is the angular distance of the echoing dust from the source.

Figures 5a-c are three different depictions of the interrelations between the delay time, and the angular and physical separations of the echoing clouds from the source assuming a source at the distance of Cas A, corresponding to  $d = 3.4 \text{ kpc}$  (Reed et al. 1995). Figure 5a shows the echo distance from the source,  $r$ , as a function of the delay time  $t$  for the separation angles  $\alpha$  corresponding to the echoes listed in Table 1. All distances are bound by the lower limit  $ct/2$  which is the minimum distance corresponding to dust located at point  $A$

immediately behind the source (see Figure 4). The vertical lines represents the maximum delay time, corresponding to  $t = 320$  yr, the age of Cas A, and a delay time of 50 yr, as suggested by Krause et al. (2005) from the analysis of the early *Spitzer* data. Figure 5b depicts the echo distance from the source as a function of angular separation. The vertical dashed lines correspond to the angular separations of the echoes listed in Table 1. The filled squares and open diamonds correspond to distances calculated for delay times of  $ct = 320$  and 50 yr, respectively. Figure 5c depicts the physical location of the echoes with respect to the source, as projected on a plane that includes the source, located at the origin  $(x, y) = (0, 0)$ , and the observer (off scale), located at  $(x, y) = (d, 0)$ . The vertical line going through the origin represents the plane of the sky going through the source. The two ellipses shown in the figure are the loci of all points with equal delay times. The filled squares and open diamonds represent the echoes listed in Table 1 assuming delay times of 320 and 50 yrs, respectively. Echo 7 with the largest separation angle from the source is almost on the plane of the sky when  $t = 320$  yr, but at a large distance in front of the source when  $t = 50$  yr.

The figures illustrate that when the delay times are short, a given range of angular distances will correspond to a wide range of echo-source distances, whereas long delay times will translate into a significantly narrower range of echo-source distances for the same range of angular distances. When  $t = 50$  yr, the range of distances,  $r$ , spanned by the echoes in Table 1 is between 27 and 1172 lyr. This range is narrowed to only 160 and 359 lyr when  $t = 320$  yr (see Table 2).

### 3. MODEL INPUT PARAMETERS

#### 3.1. The Echo Delay Time

Krause et al. (2005) suggested that the echoes were produced by a recent flaring of the neutron star that happened around 1950. Here we additionally consider the alternative scenario in which the echoes are generated about 320 yr ago by the radiative energy released following the core collapse of the progenitor star of the Cas A SN.

To discriminate between the two scenarios ( $t = 50$  or 320 yr) we determine the incident flux required to produce each echo spectrum. Since the two scenarios place the echoing dust clouds at different distances, these fluxes will translate into different burst luminosities. To check the viability of any physical scenario we require that all echoes are generated by the same burst with a single well-defined intrinsic luminosity.

### 3.2. The Burst Spectrum and Duration

Because neither the Cas A SN nor any subsequent outburst of the neutron star has been observed, we do not know the spectrum of the radiation that gave rise to the echoes. We will explore here two different possibilities: (1) an intense short duration EUV flash created when the SN shock breaks out through the surface of the star; and (2) a long duration optical light curve powered by the decay of radioactive elements formed in the SN explosion.

The existence of an intense burst of radiation created by the breakout of the SN shock wave through the stellar surface has been predicted by hydrodynamical simulations of SN explosions (Klein & Chevalier 1978; Falk 1978). However, because this flash of radiation lasts for only a few days, it has never been directly observed in any SN. Its existence was first indirectly inferred in SN1987A from the detection of narrow UV and optical emission lines from the SN (Fransson et al. 1989; Sonneborn et al. 1997). The lines arise from an equatorial ring, located about 0.7 lyr from the SN and produced by mass loss from the progenitor star that was flash-ionized by the EUV burst.

Several hydrodynamic models for the explosion of SN1987 A were constructed to fit the earliest UV and optical light curve (Woosley 1988; Ensman & Burrows 1992; Blinnikov et al. 2000). The models of Blinnikov et al. (2000) show that the burst had a peak blackbody temperature of  $\sim 10^6$  K, cooling on a timescale of days to a blackbody temperature of  $\sim 6000$  K, the H-recombination temperature in the expanding photosphere. We choose two intermediate temperatures of  $T_b = 5 \times 10^5$  and  $5 \times 10^4$  K to characterize two representative spectra of the breakout shock. The burst luminosity will be derived from model fits to the IR echoes.

The subsequent optical light curve of the SN will be characterized by a blackbody with a temperature of  $T_b = 6000$  K, characteristic of the early phases of the light curves of core collapse SNe [e.g. Woosley (1988)].

The IR spectrum of the echo depends on the spectral shape and intensity of the flux incident on the dust. The luminosities of the EUV burst and the optical light curve are free parameters that will be derived from model fits to the IR echoes. The duration of the burst only affects the thickness of the expanding light echo, and is a necessary parameter in converting the derived column density into a volume density of the radiating dust.

### 3.3. Interstellar Dust Model

We used the BARE-GR-S model of Zubko et al. (2004) to characterize the echoing interstellar dust. The model consists of a population of bare silicate and graphite grains and PAH molecules (see Table 5 in their paper). In this model, the dust-to-gas mass ratio is 0.0062, and the abundance of its various dust constituents is consistent with solar abundances constraints. The size distribution of the different dust species are depicted in Figure 19 of their paper, and the parameters of their functional forms are listed in their Table 7.

## 4. MODELING THE ECHO SPECTRA

### 4.1. The IR Emission from Stochastically Heated Dust

The observed IR flux,  $F_\nu(\lambda)$ , from an extended source of radiating dust is given by:

$$F_\nu(\lambda) = \left(\frac{\Omega}{\pi}\right) \mathcal{M}_d \left[ \int_{a_1}^{a_2} f(a) \kappa(\nu, a) \mathcal{G}_\nu(\lambda, a) da \right] \quad (2)$$

where  $\Omega$  is the angular size of the dust cloud,  $\mathcal{M}_d$  is the mass column density of the radiating dust,  $f(a)$  is the grain size distribution normalized to unity over the  $\{a_1, a_2\}$  size interval, and  $\kappa(\nu, a)$  is the mass absorption coefficient of the dust. Implicit in eq. (2) is a sum over dust composition. The term  $\kappa(\nu, a) \mathcal{G}_\nu(\lambda, a)$  in the equation is the spectral response of the dust to an incident radiation field, with  $\mathcal{G}_\nu$  given by an integral over dust temperatures  $T_d$ :

$$\mathcal{G}_\nu(\lambda, a) \equiv \int_{T_d} P(T_d) \pi B_\nu(T_d, \lambda) dT_d \quad (3)$$

where  $P(T_d)$  ( $\text{K}^{-1}$ ) is the temperature probability distribution of the stochastically heated dust, and  $B_\nu(T_d, \lambda)$  is the Planck function. For dust radiating at the equilibrium temperature  $T_d^{eq}$ ,  $P(T_d)$  collapses to the delta-function  $\delta(T_d^{eq})$ , and  $\mathcal{G}_\nu(\lambda, a) = \pi B_\nu(T_d^{eq}, a)$

### 4.2. Echo Spectra For Different Burst Models

To model the IR emission from the echoing clouds we will expose a population of interstellar dust to a burst of radiation emanating from the SN. The burst spectrum will be characterized by a blackbody at a fixed temperature  $T_b$ . A significant fraction of its soft X-rays and EUV photons will be absorbed in the intervening medium to the clouds. The optical depth,  $\tau(\nu)$ , will be parametrized by the intervening ISM column density,  $N_H$ . The



flux incident on the dust grains is then given by:

$$F_\nu^b(\lambda) = \xi F_0 \left[ \frac{\pi B_\nu(T_b, \lambda)}{\sigma T_b^4} \right] e^{-\tau(\lambda)} \quad , \quad (4)$$

where  $F_0$  is a fixed flux, calculated for a nominal luminosity  $L_0 = 1 \times 10^{12} L_\odot$  and a nominal distance of  $r_0 = 160$  lyr between the radiating dust and the source, and  $\xi$  is a model parameter determined by the flux required to fit the observed IR echo. Numerically,  $F_0$  is given by:

$$F_0 \equiv \frac{L_0}{4\pi r_0^2} = 1.33 \times 10^4 \text{ erg s}^{-1} \text{ cm}^{-2} \quad (5)$$

Since the H-column density to the echoing clouds is unknown, we will calculate the burst's attenuation for three different H-column densities given by  $N_H = 1.5 \times 10^{18}, 1.5 \times 10^{19}$ , and  $1.5 \times 10^{20} \text{ cm}^{-2}$ . For a typical echo distance of 160 lyr these column densities correspond to average ISM densities of  $n_H = 0.01, 0.1$  and  $1.0 \text{ cm}^{-3}$ , respectively.

Our model calculations were performed for seven different burst models characterized by different burst temperatures and intervening H-column densities. Models with a burst temperature of  $T_b = 5 \times 10^5 \text{ K}$  are designated as EUV models, and those with burst temperature of  $T_b = 5 \times 10^4 \text{ K}$  as UV models. Model designations include a suffix of 18, 19, or 20 corresponding to assumed SN-echo column densities of  $N_H = 1.5 \times 10^{18}, 1.5 \times 10^{19}$ , and  $1.5 \times 10^{20} \text{ cm}^{-2}$ , respectively. So model EUV19 corresponds to a burst with a temperature of  $5 \times 10^5 \text{ K}$  and a column density of  $1.5 \times 10^{19} \text{ cm}^{-2}$  to the echoing clouds. Model UV20 corresponds to a burst with a temperature of  $5 \times 10^4 \text{ K}$  and an ISM column density of  $1.5 \times 10^{20} \text{ cm}^{-2}$ . In addition we also calculated the IR echo for an optical light curve characterized by a blackbody with a temperature of 6000 K. This model is designated as OLC. We neglected any attenuation of the burst in the OLC model, because even for the highest column density the extinction was negligible.

We calculated model echo spectra for each burst model for a grid of fluxes, characterized by different values of  $\xi$  ranging from  $10^{-3}$  to 10. For example, we calculated 16 IR spectra for burst model EUV18 by varying  $\xi$  from 0.001 to 1.0 with 14 intermediate values. The only free model parameter is the normalization factor, which is equal to the dust mass column density,  $\mathcal{M}_d$ , of the model spectrum that produced the lowest value of  $\chi^2$ .

Figure 6 compares the fluxes from the different burst scenarios outlined above as they are incident on an echoing cloud at a distance of 160 lyr from the SN. For illustrative purposes, the fluxes from the EUV and UV bursts were calculated for values of  $\xi = 1.0$ , and the flux from the optical light curve was calculated for  $\xi = 0.01$ , reflecting its expected lower luminosity. For sake of comparison we added the flux of the general interstellar radiation field [ISRF; Mathis et al. (1983)].

Figures 7, 8 and 9 depict the model results for the optical light curve, and the EUV and UV burst, respectively. The top panels in the figures show the calculated IR spectra of dust that is exposed to a range of illuminating fluxes, characterized by different values of  $\xi$ . To illustrate the dependence of the spectral signature of the dust on the flux and spectral shape of the incident radiation we normalized all fluxes to unity at  $20\ \mu\text{m}$ . The middle panels depict the best fits to the echo spectra by the incident fluxes. Different echoes required exposure to different fluxes to fit their IR spectra. The bottom panels of the figures show the contributions of the different dust components to the total flux from Echo 3.

The figures show that the radiation from the optical light curve cannot reproduce the observed characteristic rise in the echo spectra between  $14$  and  $20\ \mu\text{m}$ . In contrast, both the EUV and UV bursts reproduce the echo spectra fairly well, independent of the density of the intervening medium. This fact is shown more quantitatively in Table 2 which summarizes the results of our fits. The  $\chi^2$  values of the fits of the optical light curve to the echo spectra are generally significantly higher than those for the EUV and UV fits.

The decomposition of the fits to Echo 3 into the various dust components illustrates that the rapid rise in the echo spectra between  $\sim 14 - 20\ \mu\text{m}$ , is caused by the  $18\ \mu\text{m}$  silicate feature. Two conditions have to be met to produce the observed rise in the echoes’ spectra: (1) the silicate grains have to be heated to temperatures in excess of  $\sim 150\ \text{K}$ ; and (2) the silicate emission has to dominate the emission from graphite grains which have a smooth spectrum over the  $\sim 10 - 40\ \mu\text{m}$  wavelength interval. The echoes of the optical light curve fails to meet both conditions. Silicate grains have a low opacity to optical photons and therefore remain at relatively low temperatures. The top panel of Figure 10 shows that the equilibrium silicate temperature is only about  $83\ \text{K}$  for the OLC model. Stochastic heating is limited to the smallest grains with sizes  $\lesssim 70\ \text{\AA}$ . In contrast, graphite grains have a much larger opacity at visible wavelengths and attain much higher equilibrium temperatures of  $\sim 175\ \text{K}$ . Consequently, the IR echo spectrum produced by the optical light curve is dominated by graphite emission.

The EUV and UV bursts meet both requirements for producing the rise in the echo spectra. As shown in Figure 10, they both possess sufficiently hard photons to raise the equilibrium silicate temperature to  $\sim 150\ \text{K}$ . Compared to the optical light curve, a larger fraction of the small grains are fluctuating to temperatures beyond  $\sim 100\ \text{K}$ . Furthermore, the opacity of silicate grains rises dramatically in the EUV, and becomes comparable to that of the graphite grains. Consequently, as illustrated in the bottom row of Figs. 8 and 9, the total IR spectrum is dominated by silicate emission.

## 5. MODEL RESULTS

### 5.1. Burst Scenario and Derived Burst Properties

The incident flux that provides the best fit to a given echo spectra can be converted to burst luminosity by:

$$L_b = \left( \frac{r}{r_0} \right)^2 \xi_F L_0 \quad (6)$$

where  $r$  is the *actual* distance of the particular echo from the SN,  $L_0 = 1 \times 10^{12} L_\odot$ , and  $\xi_F$  is the value of  $\xi$  that produced the best fitting incident flux.

Each echo requires a particular incident flux,  $F^b$ , to produce its IR spectrum. Given this flux, the value of  $\xi_F$  depends on the assumed column density of the intervening ISM. A higher column density will require larger values of  $\xi_F$ , corresponding to larger burst luminosities.

Figures 11 and 12 depict the burst luminosities required to produce the echo spectra for the different burst models and delay time scenarios. We assume that all echoes were produced by a single burst. A viable echo scenario should therefore give the same burst luminosity for all echoes. The results show that the echo scenario with the 50 yr delay time produces a large spread in burst luminosities, compared to the 320 yr delay scenario. The figures shows that the dispersion in the derived burst luminosities for the latter scenario is only about 50% of the mean value (see also Table 3), compared to a factor of two in the former. This is a direct consequence of the fact that the echo spectra are generally very similar requiring exposure to the same incident flux of radiation. In the  $t = 50$  yr burst scenario the echoes are spread out over a wide range of distances from the SN, leading to a wide range of burst luminosities. In other words, the echoes do not exhibit the wide range of spectral differences expected from the large variations in their distances from the SN if they were caused by a single burst of radiation. Narrowing the range of burst luminosities for the 50 yr delay model will require more distant echoes to have systematically lower column density, a non-physical and contrived solution to this problem. We therefore conclusively rule out the possibility that the echoes have a short delay time of only  $\sim 50$  yr.

Table 2 shows the model fits for each of the echoes assuming a 320 yr delay time. For each model we present the incident flux required to produce the best fit to the echo spectrum as characterized by the value of  $\xi_F$ , the burst luminosity,  $L_b$ , the column density of the echoing cloud,  $N_H$ , and the  $\chi^2$  of the fit. For each echo, the value of  $\chi^2$  was normalized to unity for the best fitting model.

From the values of the  $\chi^2$  of the fit, we see that the optical light curve provides a significantly worse fit to the echo spectra than the EUV and UV models. The EUV and

UV models are generally of similar quality, although for echoes 1, 2, and 3, UV models are distinctly better. The models with a lower H-column density usually provided slightly better fits than the models with  $N_H = 1.5 \times 10^{20} \text{ cm}^{-2}$ .

Table 3 shows the burst luminosity averaged over all echoes for each burst model. It clearly shows the correlation between the derived burst luminosity and the column density of the intervening ISM. Larger column densities require higher burst luminosities to produce the same flux needed to produce the observed echo spectrum. Excluding model results for the highest column density, we get that the average EUV-UV burst luminosity is  $L_b = 1.5 \times 10^{11} L_\odot$ .

## 5.2. Derived Cloud Properties

From the fits of the calculated IR spectra to the observations we can derive the column density,  $\mathcal{M}_d$  of the emitting dust. We take  $\Omega$  to be the width of the IRS LL slit squared,  $\Omega = (10.6'')^2$ . The corresponding H-column density is given by:  $N_H = \mathcal{M}_d / (m_H Z_{dH})$ , where  $Z_{dH} = 0.0087$  is the dust-to-H mass ratio of the BARE-SG-S Zubko et al. (2004) interstellar dust model, and  $m_H$  is the mass of the H-atom. The column densities derived for each echo and burst model are listed in Table 2. Echo 6 is the brightest, and consequently has the highest H-column density. Table 4 lists the value column density of each echo, averaged over all EUV and UV burst models. The average column density for Echoes 1-5 is about  $4.5 \times 10^{18} \text{ cm}^{-2}$ , and higher by a factor of  $\sim 4$  for Echo 6.

The IR emission arises from a narrow region along the observer’s line of sight that is illuminated by the burst of radiation. The width of the radiation front is determined by the burst duration  $\Delta t_b$ . The hydrogen number density,  $n_H$ , of the echoing cloud can be derived from the dust mass column density,  $\mathcal{M}_d$ , by:

$$n_H = \left( \frac{\mathcal{M}_d}{m_H Z_{dH}} \right) (c \tau_b)^{-1} \approx \frac{385}{\tau_b(d)} \text{ cm}^{-3} \quad (7)$$

where the numerical value was derived for an echo column density of  $N_H = 1 \times 10^{18} \text{ cm}^{-2}$ .

A cross section of the echoing clouds should show the different layers of dust heated by the evolving burst, with successively deeper layers comprising dust exposed to higher burst temperatures. The width of each layer is determined by the burst cooling time at that temperature, with longer cooling times corresponding to wider layers. Our models show that the observed  $\sim 14 - 20 \mu\text{m}$  rise in the echo spectrum can be reproduced by any burst that has sufficient UV photons, so each dust layer in the echoing cloud that was heated by the EUV-UV burst has a similar IR spectrum. The model is therefore insensitive to the details

of the evolution of the burst, and the effective width of the echoing cloud will be determined by the cooling time of the lowest burst temperature still capable of producing the observed echo spectrum. From the models of Blinnikov et al. (2000), we take this time to be about 1 d, giving an average cloud density of  $n_H \approx 385 \text{ cm}^{-3}$ .

This is a plausible density for the echoing clouds, corresponding to those of typical cirrus clouds (Wolfire et al. 2003). Cas A lies on the far side of the Perseus arm [e.g. Bieging et al. (1991)], so there are relatively few (if any) molecular clouds behind the remnant (Ungerechts et al. 2000) to reflect the radiative burst from the SN.

Since the optical light curve is incapable in producing the observed  $\sim 14 - 20 \mu\text{m}$  rise in the echo spectra, its luminosity must be significantly lower than the burst luminosity at  $\sim 2 \times 10^4 \text{ K}$ . The SN light curve must therefore rapidly decline from a value of  $\sim (1.5) \times 10^{11} L_\odot$ . Observations of SN1987A show that the bolometric luminosity of the optical light curve was only  $\sim 3 \times 10^7 L_\odot$ . If the optical light curve from Cas A experienced a similar decline in luminosity, then it made a negligible contribution to the emission spectra of the echoes.

## 6. SUMMARY

The *Spitzer* satellite discovered a series of IR echoes around Cas A that are caused by the delayed arrival of thermal emission from dust heated by the radiative output from the SN. Echo spectra are distinct from the IR emission from the diffuse ISM, exhibiting a sharp rise at wavelengths between  $\sim 14$  and  $20 \mu\text{m}$ . In hindsight, the echoes can also be found in the *IRAS* images from 1983.

We assume that the echoes are generated by the absorption and thermal reemission by interstellar dust of radiation emitted during a single epoch from the SN. We calculated the fluxes incident on the dust required to generate the observed echoes for different radiative output models of the SN. They include the optical light curve, powered by radioactive nuclei generated in the SN explosion, and a burst of EUV radiation generated by the breakout of the SN shock wave through the stellar surface.

We rule out the suggestion, based on early and spatially-limited data, that the echoes were generated by a recent, circa 1950, pulse of radiation associated with the flaring of the neutron star. Instead, the echoes were formed by radiation associated with the SN event itself that occurred about 320 yr ago. All the inner echoes are therefore located at a distance of about 160 lyr, directly behind the SN.

Our models show that the rise in the echo spectra is due to the  $18 \mu\text{m}$  silicate feature.

The silicate grains radiate mostly at the equilibrium temperature of  $\sim 120$  K and dominate the echo spectra. The optical light curve is incapable of heating the silicates to sufficiently high temperature required to reproduce the spectral characteristics of the echoes, and is therefore ruled out as the source of the echoes.

The echoes are instead generated by the intense EUV-UV burst of radiation generated by the shock breakout. We show that the echo spectra can be reproduced by bursts with a wide range of temperatures from  $\sim 5 \times 10^4$  to  $\sim 5 \times 10^5$  K. The burst luminosity required to generate the echoes depends on the assumed H-column density between the SN and the echoing cloud. We find the average burst luminosity to be  $\sim 1.5 \times 10^{11} L_{\odot}$  for an average intervening H-column density of  $\sim 1.5 \times 10^{19} \text{ cm}^{-2}$ .

The average H-column density of the echoing clouds is  $\sim 5 \times 10^{17} \text{ cm}^{-2}$ , which for a burst duration time of  $\sim 1$  d gives an average cloud density of  $\sim 400 \text{ cm}^{-3}$ . This density is typical of dense cirrus clouds, and consistent with the location of Cas A behind the Perseus arm and the paucity of dense molecular material behind the remnant.

The breakout of a shock through the stellar surface has only been indirectly inferred in SN1987A from the fluorescent line emission from its surrounding circumstellar medium. The Cas A echoes represent the first indirect "view" of a shock breakout via the thermal dust emission from echoing clouds.

ED acknowledges the support of NASA's LTSA03-0000-065. This work of F. G was supported by Research Associateship awards from the National Research Council (NRC) and the Oak Ridge Associated Universities (ORAU) at NASA Goddard Space Flight Center.

## REFERENCES

- Bieging, J. H., Goss, W. M., & Wilcots, E. M. 1991, *ApJS*, 75, 999
- Blinnikov, S., Lundqvist, P., Bartunov, O., Nomoto, K., & Iwamoto, K. 2000, *ApJ*, 532, 1132
- Bode, M. F., O’Brien, T. J., & Simpson, M. 2004, *ApJ*, 600, L63
- Bond, H. E., Henden, A., Levay, Z. G., et al. 2003, *Nature*, 422, 405
- Crotts, A. P. S. 1988, *ApJ*, 333, L51
- Dwek, E. & Felten, J. E. 1992, *ApJ*, 387, 551
- Ensmann, L. & Burrows, A. 1992, *ApJ*, 393, 742
- Falk, S. W. 1978, *ApJ*, 225, L133
- Fransson, C., Cassatella, A., Gilmozzi, R., et al. 1989, *ApJ*, 336, 429
- Fransson, C. & Lundqvist, P. 1989, *ApJ*, 341, L59
- Hines, D. C., Rieke, G. H., Gordon, K. D., et al. 2004, *ApJS*, 154, 290
- Kapteyn, J. C. 1902, *Astronomische Nachrichten*, 157, 201
- Kim, Y., Rieke, G. H., Krause, O., et al. 2008, *ArXiv e-prints*, 801
- Klein, R. I. & Chevalier, R. A. 1978, *ApJ*, 223, L109
- Krause, O., Rieke, G. H., Birkmann, S. M., et al. 2005, *Science*, 308, 1604
- Mathis, J. S., Mezger, P. G., & Panagia, N. 1983, *A&A*, 128, 212
- Panagia, N., Gilmozzi, R., Macchetto, F., Adorf, H.-M., & Kirshner, R. P. 1991, *ApJ*, 380, L23
- Reed, J. E., Hester, J. J., Fabian, A. C., & Winkler, P. F. 1995, *ApJ*, 440, 706
- Rest, A., Suntzeff, N. B., Olsen, K., et al. 2005, *Nature*, 438, 1132
- Sonneborn, G., Fransson, C., Lundqvist, P., et al. 1997, *ApJ*, 477, 848
- Thorstensen, J. R., Fesen, R. A., & van den Bergh, S. 2001, *AJ*, 122, 297
- Ungerechts, H., Umbanhowar, P., & Thaddeus, P. 2000, *ApJ*, 537, 221

Wolfire, M. G., McKee, C. F., Hollenbach, D., & Tielens, A. G. G. M. 2003, *ApJ*, 587, 278

Woosley, S. E. 1988, *ApJ*, 330, 218

Zubko, V., Dwek, E., & Arendt, R. G. 2004, *ApJS*, 152, 211



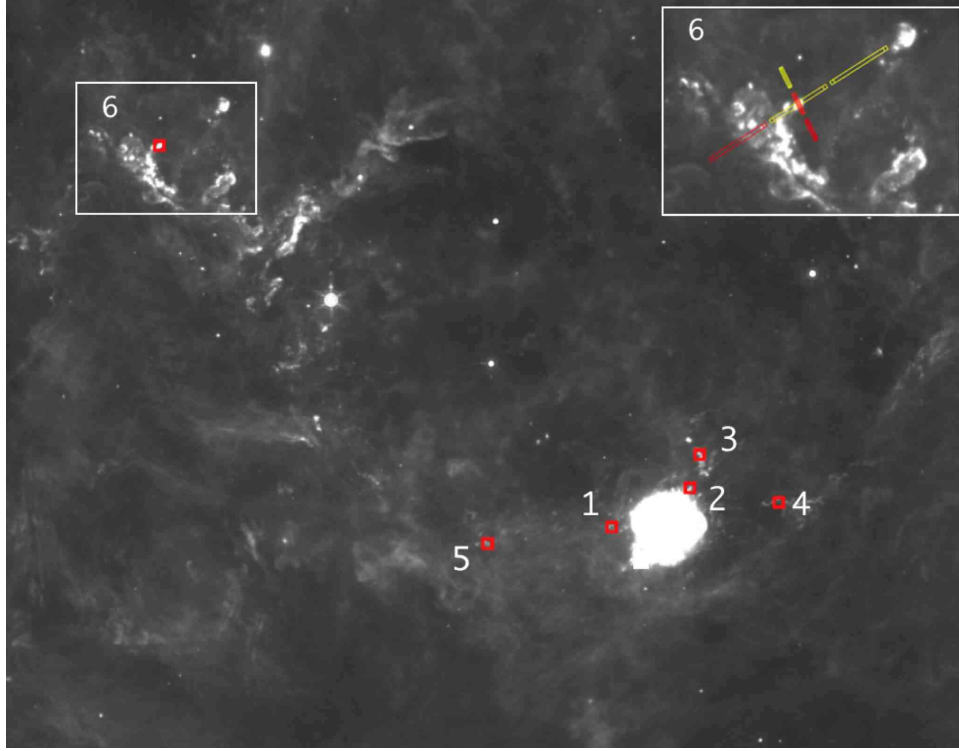


Fig. 1.— A map of the region around Cas A showing the location of all transient light signals identified as echoes (red squares). The region enclosed by a white rectangle and marked “fil” is also shown as an inset in the upper right corner of the figure. The inset shows the position of the IRS SL and LL slits.

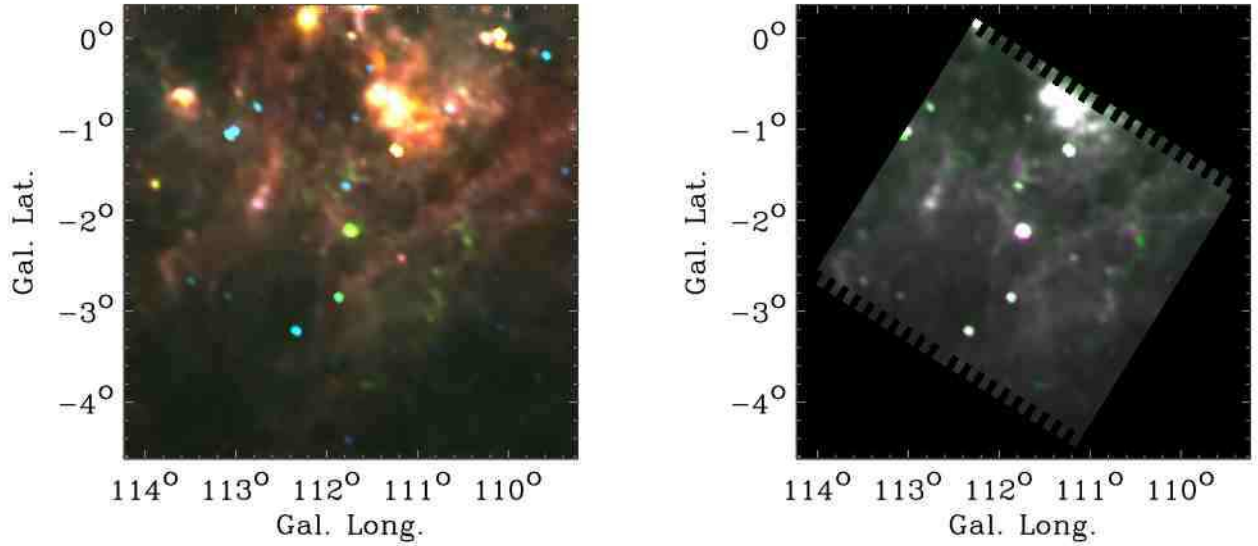


Fig. 2.— **Left panel:** This false color image displays the region around Cas A as observed by *IRAS* in 1983. Reprocessed *IRAS* data (IRIS) at 60, 25, and 12  $\mu\text{m}$  are depicted as red, green, and blue respectively. The extended structures with excess 25  $\mu\text{m}$  emission (green in color) are now known to be light echoes as they have significantly changed in *Spitzer* MIPS images in 2006. Cas A is the bright green source at the center of the image. **Right panel:** This image shows *IRAS* 25  $\mu\text{m}$  observations from 1983 in green, and *Spitzer* MIPS 24  $\mu\text{m}$  observations from 2006 in magenta. The MIPS data have been smoothed to approximate the *IRAS* spatial resolution. Cas A is the bright compact source at the center of the map. The light echoes are visible as extended structures, with magenta or green tints depending on when they were present. Nonvariable structure appears a uniform gray shade. Most of the 1983 (green) echoes seen here are also evident via their mid-IR colors as revealed in the previous figure.

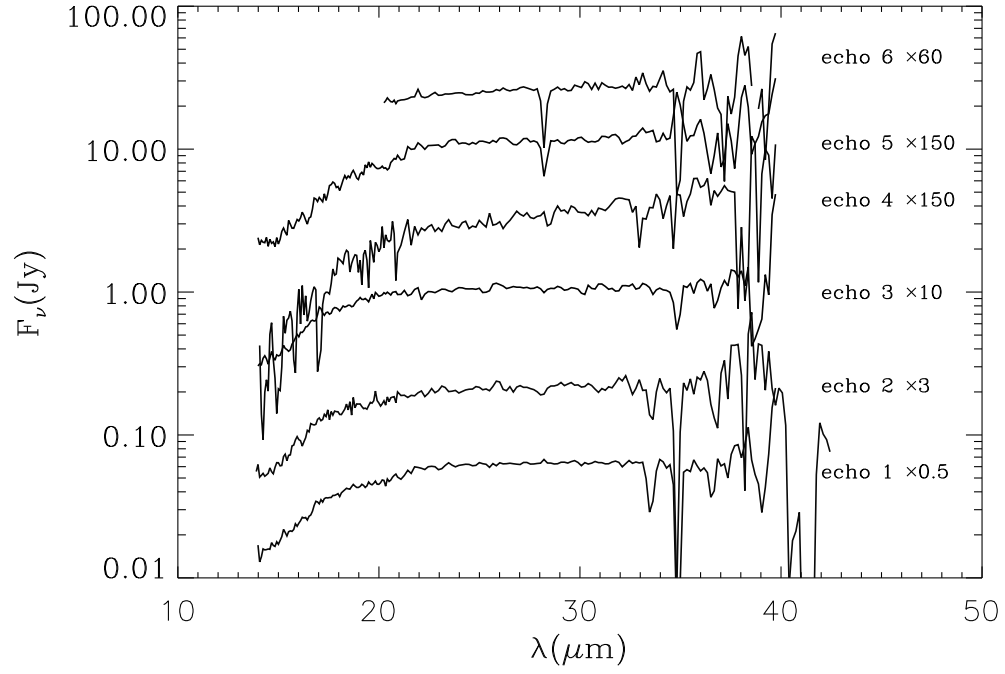


Fig. 3.— The observed spectrum of the first six echoes listed in Table 1. For echo 7 there exist only a  $24\ \mu\text{m}$  datum point at a level of XXX Jy.

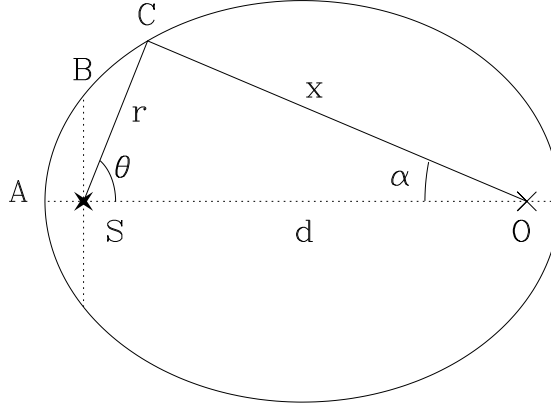


Fig. 4.— The geometry of an echo. The locus of all points with equal delay time is described by an ellipsoid with the source "S" and the observed "O" at the focal points. The lengths  $\overline{AS} = ct/2$ , and  $\overline{BS} = ct$ , where  $t$  is the difference between the observing and the emission time of a given photon. The point "C" is an arbitrary point on the ellipse sustaining an angular distance  $\alpha$  from the source, located at distances  $r$  and  $x$  from the source and observer, respectively. The length  $\overline{OS} = d$ , the distance of the source from the observer.

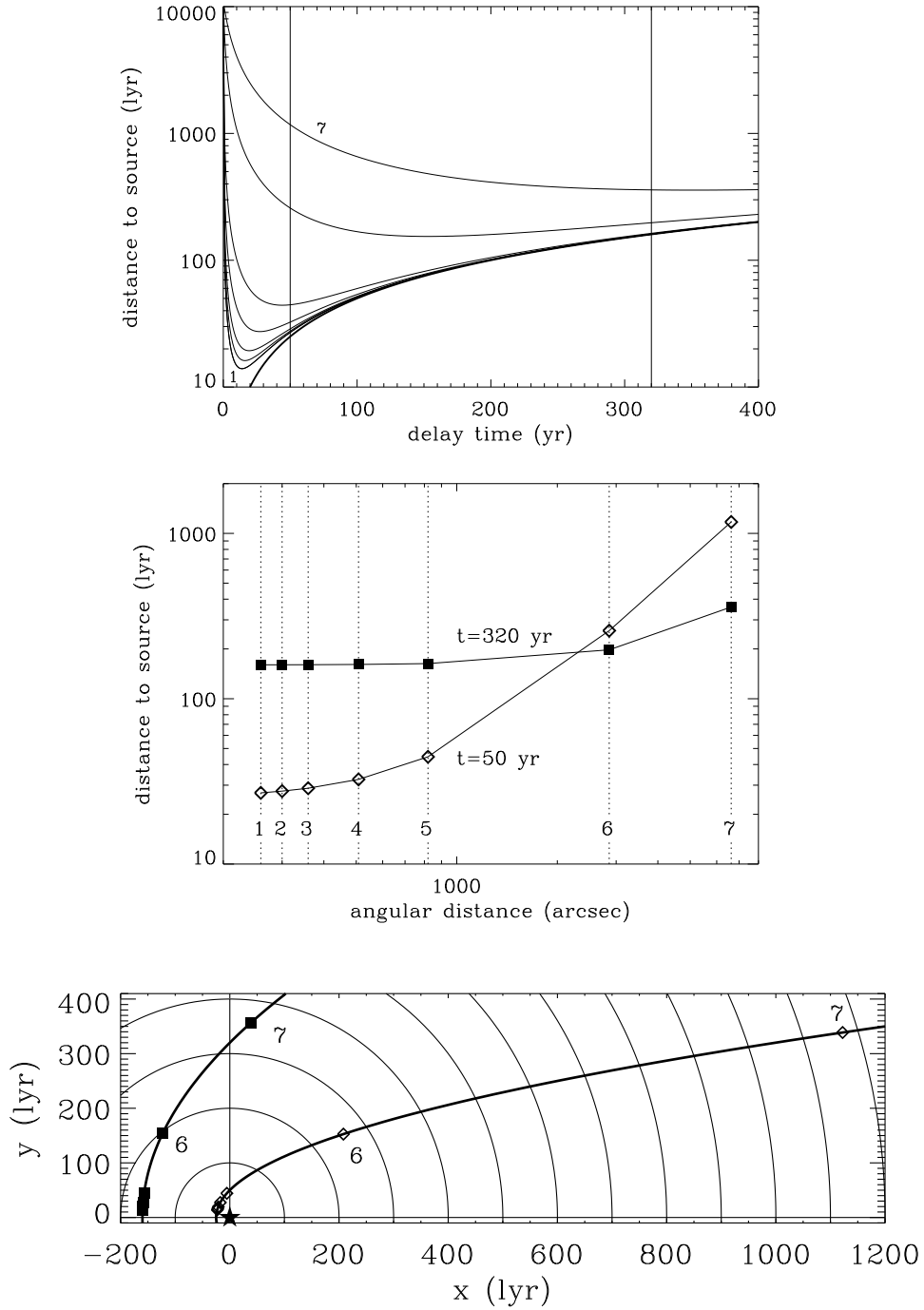


Fig. 5.— Three different depictions of the interrelations between the delay time, and the angular and physical separations of the echoing clouds listed in Table 1 from the source. The relation between the different quantities is given by eq. (1) for  $d = 3.4$  kpc, the distance to Cas A. **Top:** Echo distance to the source versus the delay time for different angular separations. **Middle:** echo distances to the source as a function of angular distance for delay times of 50 and 320 yr. **Bottom:** Physical location of the echoes with respect to the source, as projected on a plane that includes the source, located at (0,0), and the observer (off scale), located at ( $d$ ,0). All figures are described in more detail in §2.3 of the text.

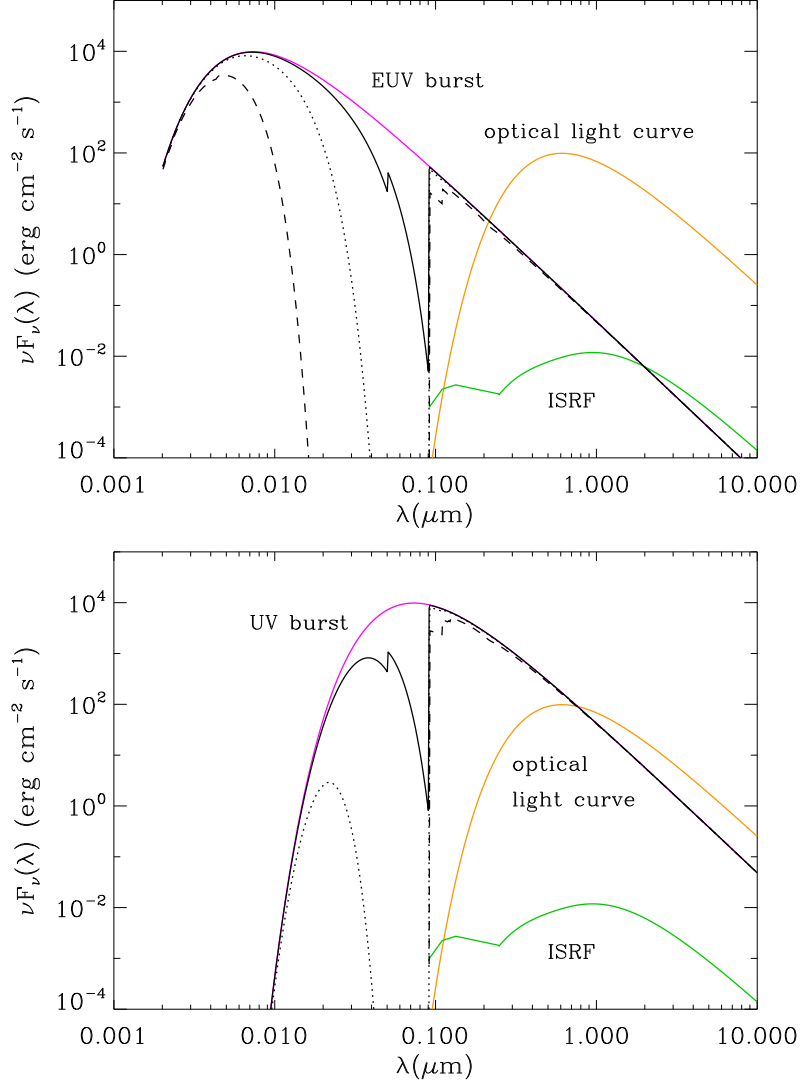


Fig. 6.— The flux of the different burst models considered in this paper (§4.2): the EUV burst (top panel), and the UV burst (bottom panel). Also shown in the figure is the specific flux from the optical light curve. For comparison, we also included the flux of the ISRF. The intrinsic luminosities of the EUV and UV burst were taken to be  $10^{12} L_{\odot}$ . The luminosity of the optical light curve was taken to be  $10^{10} L_{\odot}$ . All fluxes were calculated for a distance of 160 ly. The unattenuated burst is shown as a violet line, and the solid, dotted, and dashed line represent the flux attenuated en route to the echoing cloud by the ISM with densities of 0.01, 0.1, and  $1.0 \text{ cm}^{-2}$ , respectively. Detailed burst parameters are described in the text.

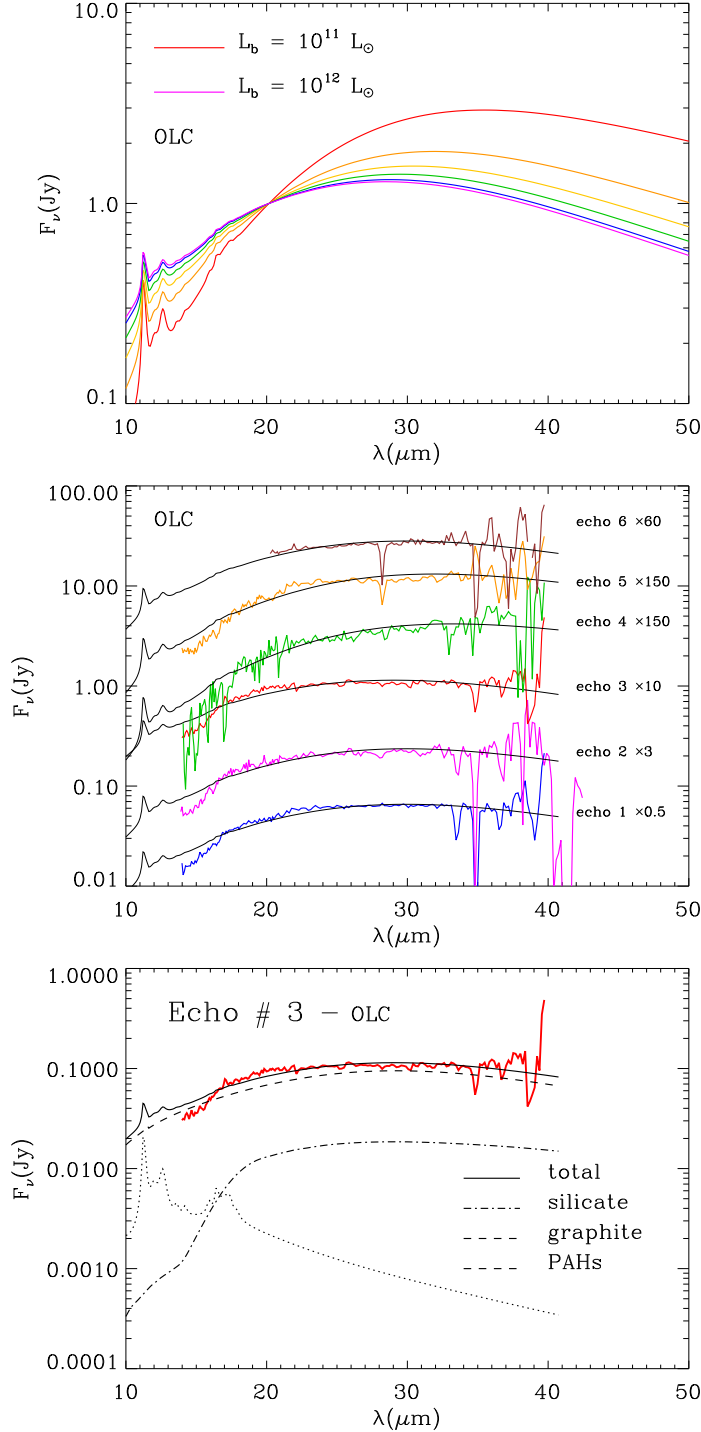


Fig. 7.— Model fits for the optical light curve (OLC). **Top row:** Calculated IR spectra of an echo exposed to different fluxes  $F_\nu^*$  characterized the product  $\xi L_0$  and calculated for  $r_0 = 160$  lyr (see eq. 4) with  $\xi = 0.1, 0.3, 0.5, 0.7, 0.9$ , and  $1.0$ . All fluxes were calculated for  $r_0 = 160$  lyr (see eq. 4) and are normalized to unity at  $\lambda = 20 \mu\text{m}$ . **Middle row:** Best fit models to the IR echoes. **Bottom row:** Decomposition of the best fitting IR spectrum of Echo 3 into its emission components from silicate and graphite grains and PAHs. The figure illustrates the failure of the OLC to fit the echo spectra. A detailed discussion of the figure is in the text.

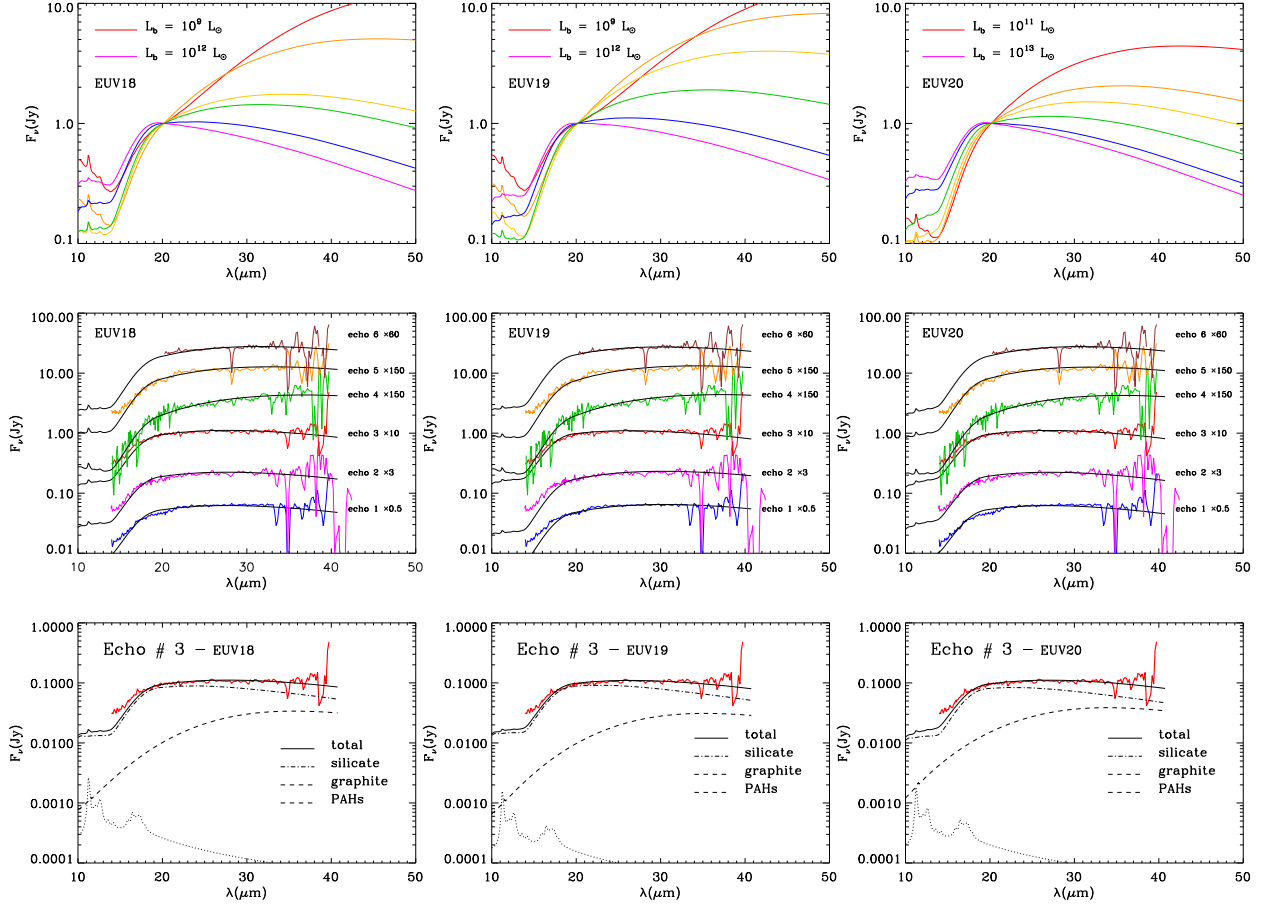


Fig. 8.— Model fits for the EUV burst model propagating through a densities of 0.01 (left column), 0.10 (middle column), and  $1.0 \text{ cm}^{-3}$  (right column). **Top row:** Calculated IR spectra of an echo exposed to different fluxes characterized by values of  $\xi = 0.001, 0.008, 0.06, 0.10, 0.40$ , and  $1.0$  (left panel);  $\xi = 0.001, 0.006, 0.02, 0.08, 0.40$ , and  $1.0$ ; and  $\xi = 0.1, 0.4, 0.8, 2.0, 6.0$ , and  $10$ . All fluxes were calculated for  $r_0 = 160 \text{ lyr}$  (see eq. 4) and are normalized to unity at  $\lambda = 20 \text{ }\mu\text{m}$ . **Middle row:** Best fit models to the IR echoes. **Bottom row:** Decomposition of the best fitting IR spectrum of Echo 3 into its emission components from silicate and graphite grains and PAHs. A detailed discussion of the figure is in the text.



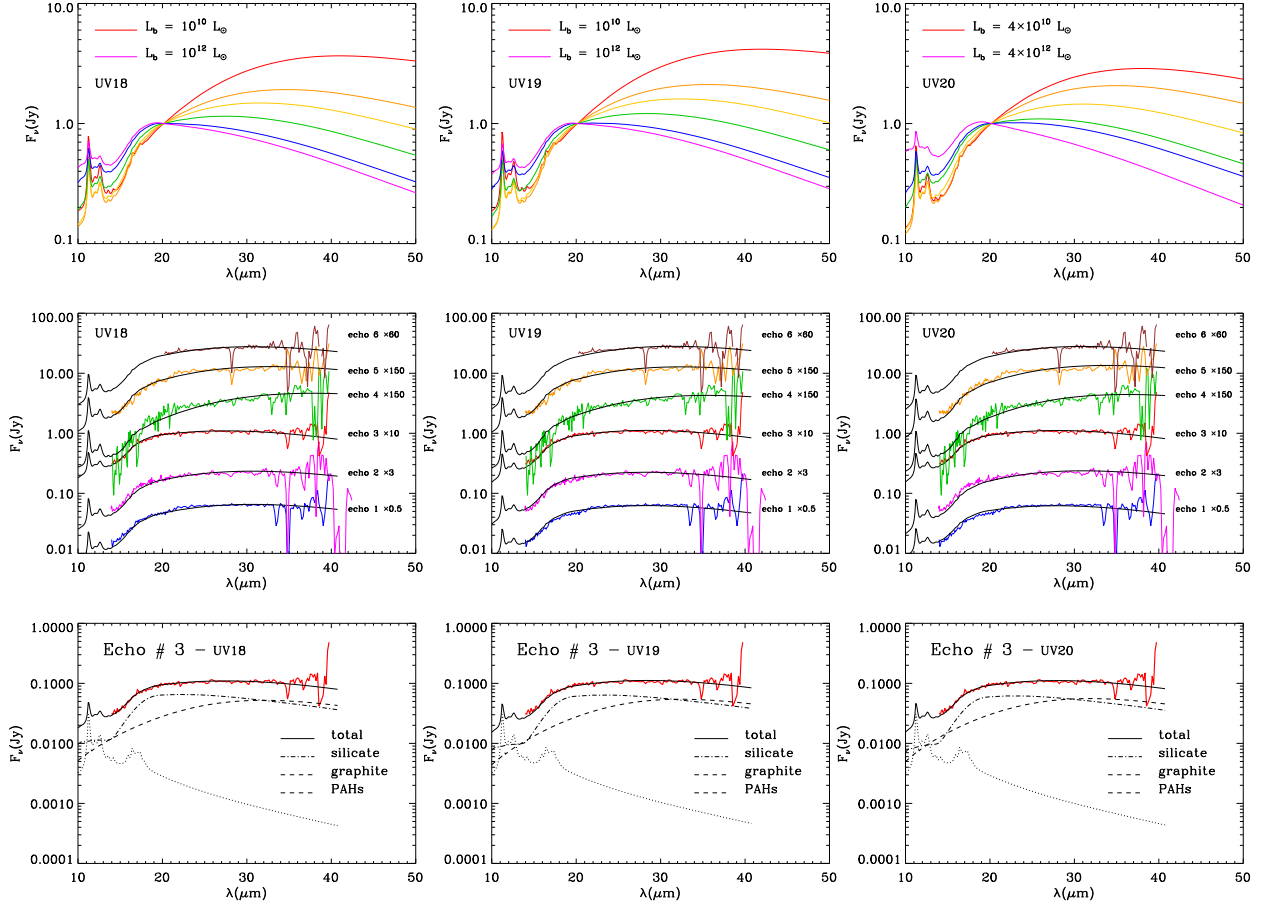


Fig. 9.— The same as Figure 8 for the UV burst model. Calculated IR spectra of an echo exposed to different fluxes characterized by values of  $\xi = 0.01, 0.04, 0.08, 0.20, 0.60$ , and  $1.0$  (left and middle panel); and  $\xi = 0.04, 0.08, 0.20, 0.60, 1.0$ , and  $4.0$ . All fluxes were calculated for  $r_0 = 160$  lyr (see eq. 4) and are normalized to unity at  $\lambda = 20 \mu\text{m}$ . **Middle row:** Best fit models to the IR echoes. **Bottom row:** Decomposition of the best fitting IR spectrum of Echo 3 into its emission components from silicate and graphite grains and PAHs. A detailed discussion of the figure is in the text.

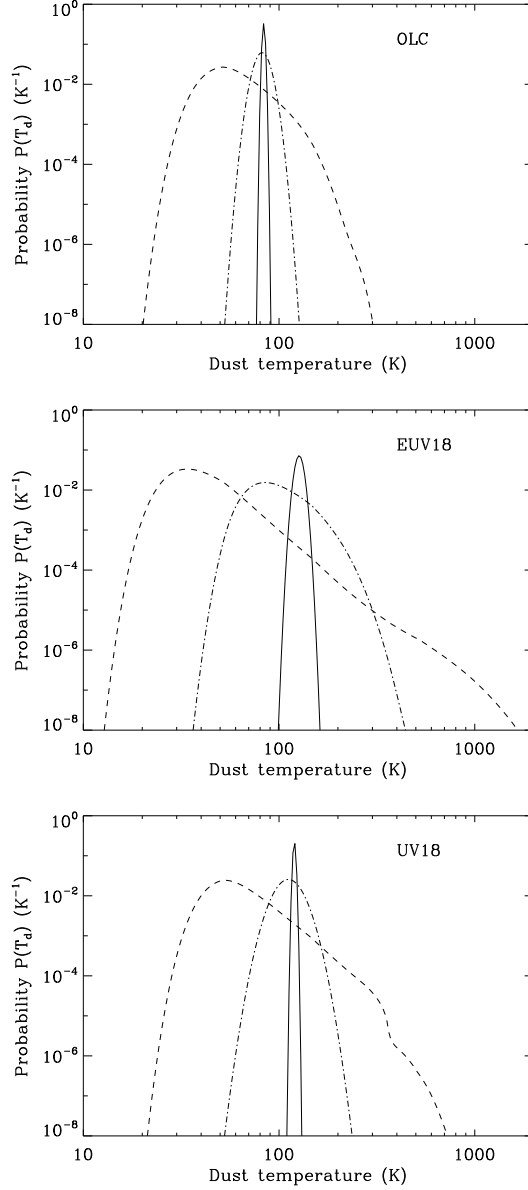


Fig. 10.— The temperature probability distribution  $P(T_d)$  ( $\text{K}^{-1}$ ) for  $0.0010 \mu\text{m}$  (dashed line);  $0.0030 \mu\text{m}$  (dashed-dotted line), and  $0.010 \mu\text{m}$  (solid line) silicate grains exposed to the optical light curve (top panel), burst model EUV18 (middle panel), and burst model UV18 (bottom panel) with fluxes calculated for  $\xi = 0.6, 0.2$ , and  $0.1$ , respectively [see eq. 4]. Larger grains radiate at the equilibrium dust temperature. Only the EUV and UV burst are capable of heating a significant fraction of the silicate grains to the temperatures ( $\gtrsim 100 \text{ K}$ ) that are needed to produce the  $18 \mu\text{m}$  feature. A more detailed discussion of the figure is in the text.

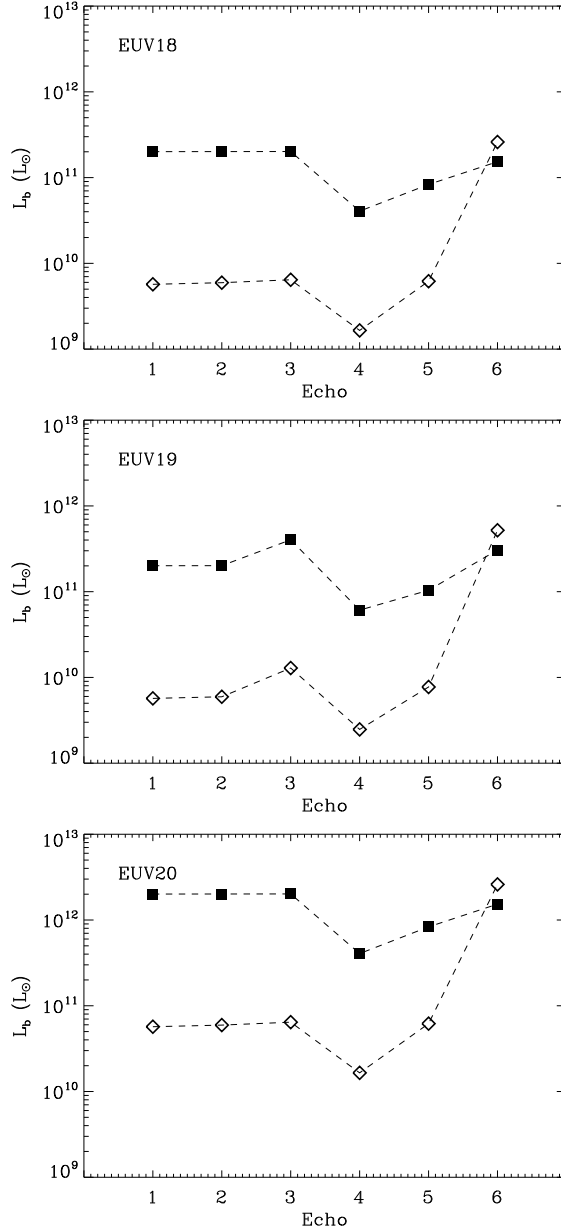


Fig. 11.— The EUV burst luminosities required to generate the IR echoes from Cas A [see eq. (6)] for different values of the density of the ISM around Cas A:  $n_H = 0.01 \text{ cm}^{-3}$  (top panel);  $n_H = 0.1 \text{ cm}^{-3}$  (middle panel); and  $n_H = 1.0 \text{ cm}^{-3}$  (bottom panel). Filled squares are values calculated for a delay time of 320 yr, whereas the open diamonds are calculated for a delay time of 50 yr. A viable model should give a single value for  $L_b$  for all echoing clouds. The scenario in which the delay time is 360 yr is more physical, since it produces a significantly narrower range of burst luminosities compared to the 50 yr model. The spread in burst luminosities in  $t=320$  yr scenario may reflect the variations in the burst attenuation en route to the echoing cloud.

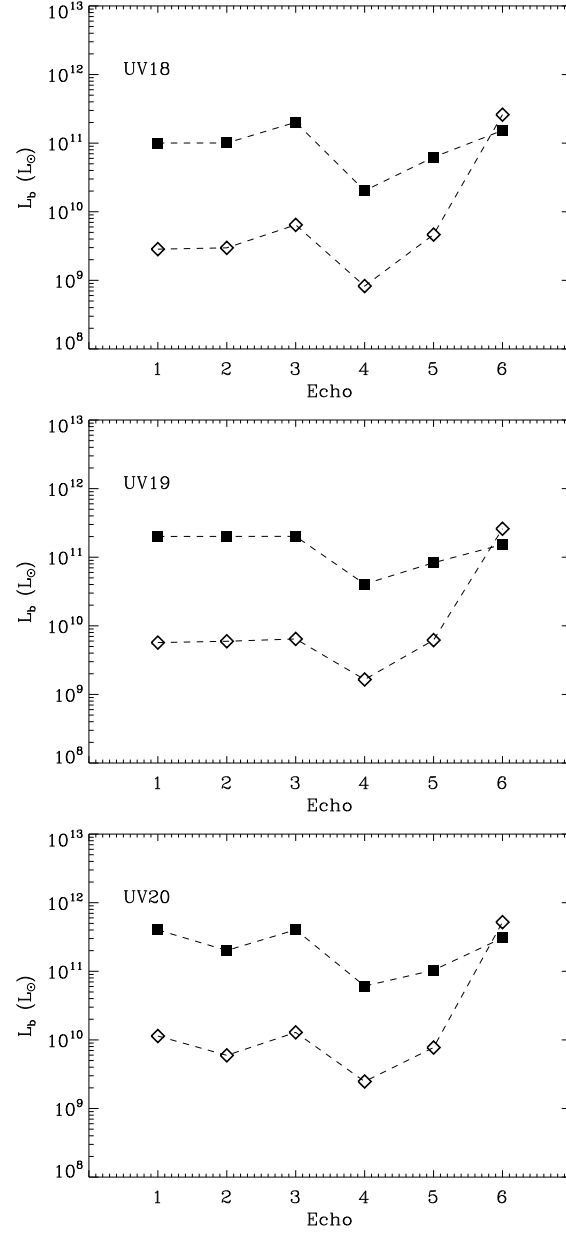


Fig. 12.— Same as Figure 11 for the UV burst.

Table 1. Observed Properties of Echoing Clouds

Target	Location (RA: DEC)	$\alpha$ (") <sup>1</sup>	$r_{50}$ (lyr) <sup>2</sup>	$r_{320}$ (lyr) <sup>3</sup>
Echo 1	23h23'38.57": +58d52'54.4"	259"	27.0	160.3
Echo 2	23h22'50.58": +58d47'30.6"	300"	27.6	160.4
Echo 3	23h22'41.55": +58d48'37.0"	359"	28.7	160.6
Echo 4	23h22'50.98": +58d41'49.4"	508"	32.5	161.2
Echo 5	23h24'12.37": +59d01'12.8"	820"	44.5	163.1
Echo 6	23h21'39.96": +59d34'26.9"	2860"	258	198
Echo 7	23h26'38.62": +57d01'19.4"	6630"	1172	359

<sup>1</sup>Angular distances were calculated from the optical expansion center located at (RA: DEC) = (23h23'27.77": +58d48m49.4s) (Thorstensen et al. 2001)

<sup>2</sup>Echo distances from the SN for a delay time of  $t = 50$  yr.

<sup>3</sup>Echo distances from the SN for a delay time of  $t = 320$  yr.

Table 2. Derived Model Properties<sup>1</sup>

Echo #		1	2	3	4	5	6
OLC:	$\xi_F$	0.6	0.6	0.8	0.2	0.3	0.6
	$L_b$	0.60	0.60	0.81	0.20	0.31	0.92
	$N_H$	2.7	1.6	1.9	1.3	3.0	9.7
	$\chi^2$	2.20	2.46	4.62	1.81	1.72	1.31
EUV18:	$\xi_F$	0.2	0.2	0.2	0.04	0.08	0.1
	$L_b$	0.20	0.20	0.20	0.041	0.083	0.15
	$N_H$	4.7	2.8	4.2	4.4	7.1	32.0
	$\chi^2$	1.67	1.66	3.98	<b>1.00</b>	1.03	1.13
EUV19:	$\xi_F$	0.2	0.2	0.4	0.06	0.1	0.2
	$L_b$	0.20	0.20	0.40	0.06	0.10	0.31
	$N_H$	7.7	4.6	3.5	4.9	9.5	26.9
	$\chi^2$	2.40	2.94	3.21	1.05	1.40	<b>1.00</b>
EUV20:	$\xi_F$	2.0	2.0	2.0	0.4	0.8	1.0
	$L_b$	2.0	2.0	2.0	0.41	0.83	1.53
	$N_H$	3.5	2.1	3.1	3.2	5.2	23.8
	$\chi^2$	1.93	1.74	3.16	1.03	<b>1.00</b>	1.10
UV18:	$\xi_F$	0.1	0.1	0.2	0.02	0.06	0.1
	$L_b$	0.10	0.10	0.20	0.020	0.062	0.15
	$N_H$	5.8	3.5	2.8	5.4	5.9	20.6
	$\chi^2$	<b>1.00</b>	1.52	<b>1.00</b>	1.64	1.10	1.09
UV19:	$\xi_F$	0.2	0.2	0.2	0.04	0.08	0.1
	$L_b$	0.20	0.20	0.20	0.041	0.083	0.15
	$N_H$	3.6	2.2	3.2	3.2	5.3	24.0
	$\chi^2$	1.14	<b>1.00</b>	1.45	1.28	1.07	1.29
UV20:	$\xi_F$	0.4	0.2	0.4	0.06	0.1	0.2
	$L_b$	0.40	0.20	0.40	0.061	0.10	0.31
	$N_H$	3.0	3.4	2.7	3.5	6.9	20.0
	$\chi^2$	1.50	2.23	1.17	1.41	1.61	1.22

<sup>1</sup> $\xi_F$  is the value of  $\xi$  [see eq. (4)] that gives the best fitting incident flux [eq. (6)]. Burst luminosities are in units of  $10^{12} L_\odot$ , and echo column densities are in units of  $10^{17} \text{ cm}^{-2}$ . For each echo  $\chi^2$  is renormalized to 1.00 for the best fitting model.

Table 3. Average Burst Luminosities<sup>1</sup>

Burst Model	$\langle L_b \rangle$ ( $10^{12} L_\odot$ )	$\sigma$ ( $10^{12} L_\odot$ )
OLC	0.57	0.28
EUV18	0.15	0.070
EUV19	0.21	0.13
EUV20	1.47	0.70
UV18	0.11	0.064
UV19	0.15	0.07
UV20	0.25	0.15

<sup>1</sup> $\langle L_b \rangle$  is the value of  $L_b$  averaged over all echoing clouds for each burst model, and  $\sigma$  is the r.m.s. dispersion of the value.

Table 4. Average Echo Column Densities<sup>1</sup>

Echo #	$\langle N_H \rangle$ ( $10^{17} \text{ cm}^{-2}$ )	$\sigma$ ( $10^{17} \text{ cm}^{-2}$ )
1	4.7	1.8
2	3.1	0.9
3	3.3	0.6
4	4.1	1.0
5	6.7	1.6
6	24.5	4.4

<sup>1</sup> $\langle N_H \rangle$  is the value of  $N_H$  averaged over all EUV-UV burst models for each echo, and  $\sigma$  is the r.m.s. dispersion of the value.